NIST Advanced Manufacturing Series
NIST AMS 100-66

Design and Calibration of the Fundamentals of Laser-Matter Interaction (FLaMI) Powder Bed Fusion Testbed at the National Institute of Standards and Technology

David Deisenroth
Sergey Mekhontsev
Steven Grantham

This publication is available free of charge from:
https://doi.org/10.6028/NIST.AMS.100-66

NIST NATIONAL INSTITUTE OF STANDARDS AND TECHNOLOGY
U.S. DEPARTMENT OF COMMERCE

NIST Advanced Manufacturing Series
NIST AMS 100-66

Design and Calibration of the Fundamentals of Laser-Matter Interaction (FLaMI) Powder Bed Fusion Testbed at the National Institute of Standards and Technology

David Deisenroth
Sergey Mekhontsev
Intelligent Systems Division
Engineering Laboratory

Steven Grantham
Sensor Science Division
Physical Measurement Laboratory

This publication is available free of charge from:
https://doi.org/10.6028/NIST.AMS.100-66

February 2025

U.S. Department of Commerce
Jeremy Pelter, Acting Secretary of Commerce

National Institute of Standards and Technology
Craig Burkhardt, Acting Under Secretary of Commerce for Standards and Technology and Acting NIST Director

NIST AMS 100-66
February 2025

Certain equipment, instruments, software, or materials, commercial or non-commercial, are identified in this paper in order to specify the experimental procedure adequately. Such identification does not imply recommendation or endorsement of any product or service by NIST, nor does it imply that the materials or equipment identified are necessarily the best available for the purpose.

Publication History
Approved by the NIST Editorial Review Board on 2025-02-20

How to Cite this NIST Technical Series Publication
Deisenroth D, Mekhontsev S, Grantham S (2025) Design and Calibration of the Fundamentals of Laser-Matter Interaction (FLaMI) Powder Bed Fusion Testbed at the National Institute of Standards and Technology. (National Institute of Standards and Technology, Gaithersburg, MD), NIST Advanced Manufacturing Series (AMS) NIST AMS 100-66. https://doi.org/10.6028/NIST.AMS.100-66

Author ORCID iDs
David Deisenroth: 0000-0002-6869-7970
Sergey Mekhontsev: 0000-0001-7764-630X
Steven Grantham: 0000-0002-8218-512X

Contact Information
david.deisenroth@nist.gov

Abstract

The advantages of additive manufacturing of metal components through laser-based powder bed fusion of metals (PBF-LB/M) have been increasingly embraced across a variety of industries and applications. But, broader adoption of this manufacturing technology requires that computational models and in-situ monitoring of such processes be experimentally validated under highly controlled conditions with advanced metrology. Such validation of models and in-situ monitoring systems are especially important for critical applications that require qualification and certification. Such controlled conditions and advanced metrology cannot be readily implemented in commercial PBF-LB/M machines due to a variety of constraints and unknowns about machine performance. Therefore, a laboratory testbed has been developed to study the Fundamentals of Laser-Matter Interaction (FLaMI) at the National Institute of Standards and Technology (NIST). This paper outlines the materials and methods to develop such a system, as well as to accurately calibrate and characterize the machine performance.

Keywords

Metal additive manufacturing; laser powder bed fusion; machine qualification; process monitoring; laser beam metrology.

Table of Contents

List of Tables

List of Figures

1. Introduction

A growing number of applications can potentially benefit from additive manufacturing by laser powder bed fusion (PBF-LB/M) [1]. But, increased adoption—especially for critical applications that require qualification and certification—requires computational models that can accurately connect processing conditions with material structure and performance of parts that are built with this manufacturing method [2]. Such models must be validated against rigorous experimental data. In parallel, process monitoring is essential for sensing defect formation in-situ, which must be supported by causal relationships between monitored response and the physics of defect formation [3]. And so, there is a significant need for fundamental studies of laser-matter interaction physics with advanced metrology under highly controlled conditions.

The highly-dynamic and microscopic characteristics of the laser-matter interaction processes used in PBF-LB/M most often necessitates high-speed, non-contact, optical metrology. Measurements of interest include melt pool thermography [4], reflected laser power and its directional distribution [5–7], as well as high-speed imaging of the spatial and spectral distribution of the byproducts plume and process ejecta [8, 9]. In order to maximize the value of the in-situ data, it must be reported quantitatively in physically accurate units. Furthermore, the laser processing conditions under which the fundamental studies are conducted must be reported in physically accurate units with associated measurement uncertainties.

Commercial PBF-LB/M machines typically do not offer direct control of the laser processing parameters or high-speed synchronization with external measurement devices. Furthermore, commercial machines are primarily designed for printing parts leaving very limited space within the build chamber for instrumentation. And so, the Fundamentals of Laser-Matter Interaction (FLaMI) testbed has been developed at the National Institute of Standards and Technology (NIST).

The FLaMI system was designed for calibrated laser scans that are highly instrumented. As such, the system works primarily with single lines and/or pads on bare plates or with a single layer of manually spread powder (with guide shims). The FLaMI system is outfitted with a state-of-the art laser, optics, and galvanometer that show excellent performance under a variety of conditions. This paper outlines the materials and methods to develop such a system, and then to calibrate and characterize the machine performance. After describing the design in Section 2, this document loosely follows the structure of ISO/ASTM 52941:2020(E) [10], while detailing the metrology used for such “acceptance tests.” Appendix A provides examples of the in-situ metrology that the FLaMI testbed can be equipped with.

2. Design

2.1. Reference plane

Establishment of a reference plane is essential to ensure consistent and well-characterized laser performance around the build area. The foundation of the reference plane is a granite base rated for nominal flatness within ± 1.3 µm around its 914 mm × 914 mm working area. Two linear rails with no-load maximum straightness deviation of less than ± 25 µm are mounted on the granite. The linear rails each host a precision linear guide bearing that carries a third linear rail with another precision guide bearing to form an X-Y gantry.

The gantry carries a precision laser distance finder such that the distance finder can be located in all X-Y positions of interest around the build area. A stainless-steel fiducial marker post can be positioned around the working area of the granite base to locate the fiducial plane approximately 240 mm above the granite. The laser distance finder has a maximum error of ± 2.5 µm. It has been found empirically that the combined imperfections of the granite, rails, bearings, and distance finder result in the ability to locate a fiducial plane within a standard uncertainty of ± 15 µm (k = 1, Type A) around the build area.

A precision X-Y digital level (manufacturer stated accuracy of ± 0.015°) is then used to transfer the granite plane to the f-theta lens plane, ensuring parallelism of the f-theta lens with the granite plane. Finally, the location of the beam waist is located relative to the f-theta lens, as well as in the critical working positions around the build plane, as discussed in Section 3.3. The method for establishing the planes discussed here is summarized in Fig. 1.

An additional design consideration is that the sample can be located relative to the laser position with X, Y, and Z stages. A further design consideration is that to ensure temporal stability, the scanner is mounted on carbon-fiber posts that are specifically designed for minimal thermal expansion, on the order of 0.5 µm/(m K). The basic system architecture is illustrated in Fig. 2.

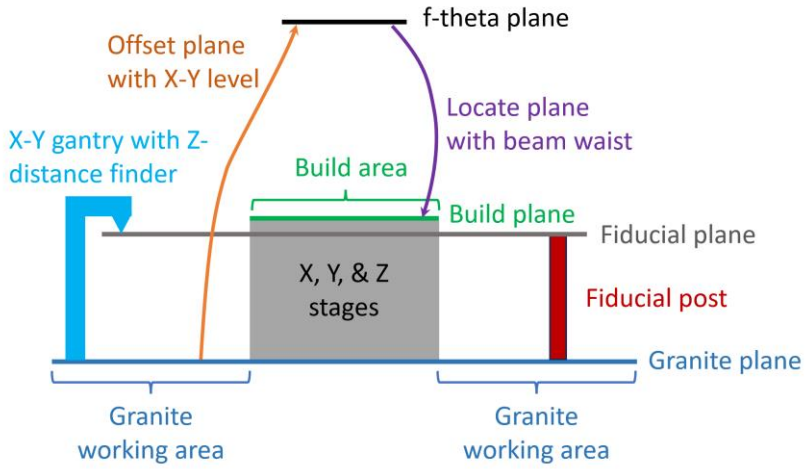

Fig. 1. Illustration of establishing the fiducial plane, the f-theta plane, and the build plane.

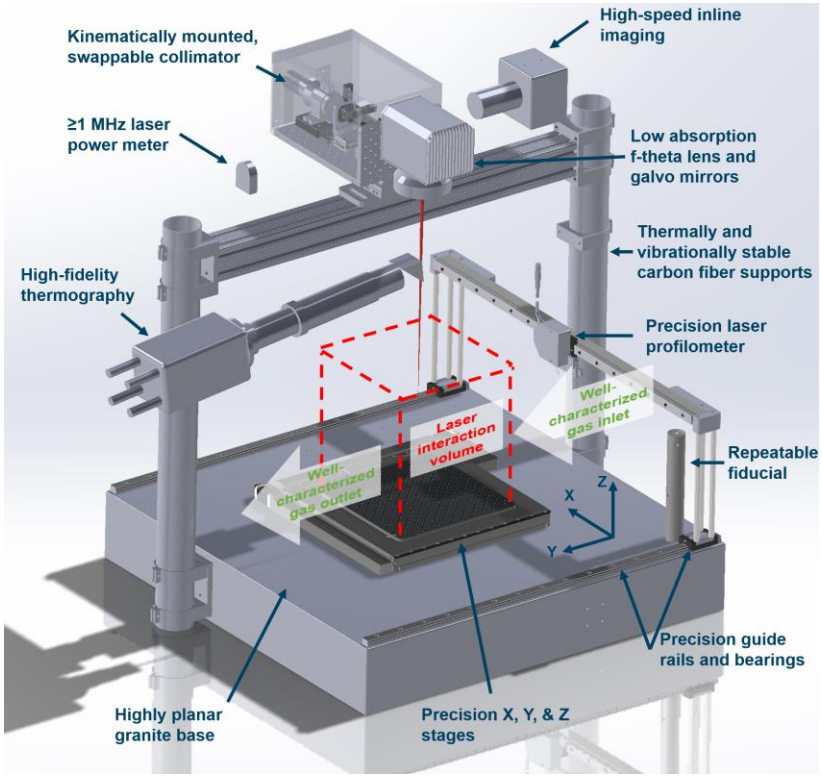

Fig. 2. Illustration of the general configuration of the FLaMI testbed.

2.2. Laser optics and integral metrology

The laser optics include a very low-absorption f-theta lens and galvanometer (galvo) mirrors optimized for the Yb-doped fiber laser central wavelength of 1070 nm. A commercially available beam splitter allows for two additional functionalities: 1) the reflected beam power from the first surface of the splitter (on the order of 0.1 %) can be used with a ≥ 1 Mhz photodetector to monitor dynamic beam power, and 2) the beam splitter allows for inline thermal imaging with a high-speed camera. The high-speed camera is primarily used in the wavelength range of 800 nm to 900 nm, but other wavebands may be implemented. The laser optics (collimator and beam splitter) are contained within a compact laser-shielding enclosure behind the galvo, while the entire FLaMI system is surrounded by a 1.22 m × 1.22 m × 2.44 m laser-safe, interlocked enclosure.

The remainder of this document roughly follows the sequence of “acceptance tests” outlined in ISO/ASTM 52941:2020(E) [10], while detailing the experimental methods used for those tests/calibrations.

3. Laser beam tests

The FLaMI system has been tested with two different single-mode fiber lasers: one with nominal maximum output of 500 W, and one with nominal maximum output of 1 kW. Some comparisons between the lasers' performances will be shown in the remainder of this section.

3.1. Laser power

Power calibration uses a commercially available air-cooled thermal power meter, which is traceable to NIST's laser power calibration laboratory. The device requires 30 s of continuous, static power and the manufacturer states that the accuracy is ± 5 % of the measured value, which is assumed to be the expanded uncertainty (k = 2) of the power measurement.

During testing, the thermal power meter absorber is located approximately 75 mm from the f-theta lens to assure that the beam diameter is large (on the order of 6 mm) to avoid exceeding the optical flux damage threshold of the power meter absorber. The thermal power meter is limited to 600 W, and so in order to assure the linearity of delivered laser power with input command bit level in the control program, data from the co-axial power monitoring (PM) photodetector (illustrated in Fig. 2) was utilized to measure powers exceeding 600 W. As shown in Fig. 3, the commanded bit level is highly linear with the output laser power measured by the thermal power meter. The bit level is based on an 8-bit scale, which provides for approximately ± 1 W resolution per commanded bit level with a 500 W laser, or ± 2 W with a 1 kW laser.

The power output measured by the PM photodetector is also highly linear and in excellent agreement with the thermal power meter, which allows for extrapolation of the calibration to 1 kW with comparable standard uncertainty (k = 1) of the power measurement. The root-mean squared error of the thermal power meter curve fit was ± 4.1 W and the same for the PM photodetector was ± 8 W.

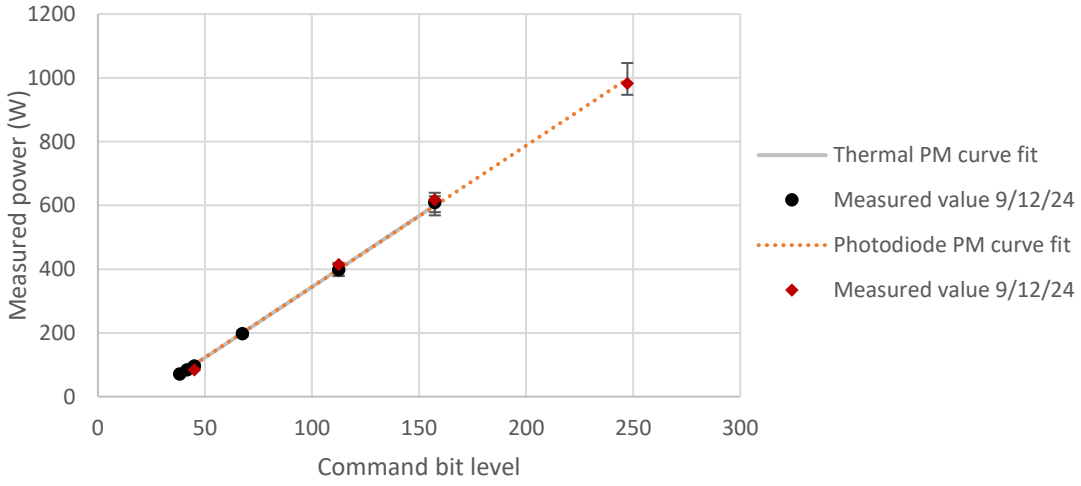

Fig. 3. Measured laser power output as a function of control program bit level with a thermal power meter, as well as a PM photodiode.

3.2. Laser power stability

As mentioned in the Introduction, the FLaMI system is used for single lines and pads, typically with no more than five tracks per pad, and typically with 30 s or more between pads. And so, the procedure detailed in ISO/ASTM 52941:2020(E) [10] does not accurately represent the operating conditions of the FLaMI laser system. The procedure detailed in ISO/ASTM 52941:2020(E) [10], which uses ISO 11554 [11] as reference, calls for a 'warm-up time' either specified by the laser vendor, or measured "not later than 2 min after laser is held at the maximum-rated-laser power for 15 min minimum." In contrast, FLaMI standard operations are brief and do not utilize a laser warm-up period, therefore it is not used during FLaMI laser characterization. In this study, two quantities related to laser stability are reported: standard deviation of measured laser power across a five melt-track pad and the laser rise and fall time.

The inline PM photodetector was used to quantify the stability of the delivered laser power. As shown in Fig. 4a, there was no appreciable trend in power from line to line across five lines at 285 W. As shown previously, laser power is linear with photodetector signal, with some noise generated by the combination of the laser system itself, the photodetector, and the data acquisition system. The percent standard deviation of the laser power about the mean at four power levels is tabulated in Table 1 for the 500 W and 1 kW lasers. The standard deviation of the delivered power of both lasers is less than ±1 %, with standard deviation decreasing as power level increases.

Another measurable quantity related to laser power stability is the laser rise and fall time. As illustrated in Fig. 4b for the case of 285 W, the 500 W laser requires 14 μs 'rise time' for the power to reach 95 % of the nominal value from 0 W. To quantify fall time, the converse quantity is measured, which is the time for the power to fall from its nominal value to 5 % of the nominal value. The rise and fall times at four power levels with both the 500 W and 1 kW laser are tabulated in Table 1. It can be observed that the rise time generally decreases as the power level increases, while the fall time increases as the power level increases. The 1 kW laser requires longer rise time than the 500 W laser, but shorter fall times. In all cases, the laser reaction time (rise or fall) is no more than 40 μs.

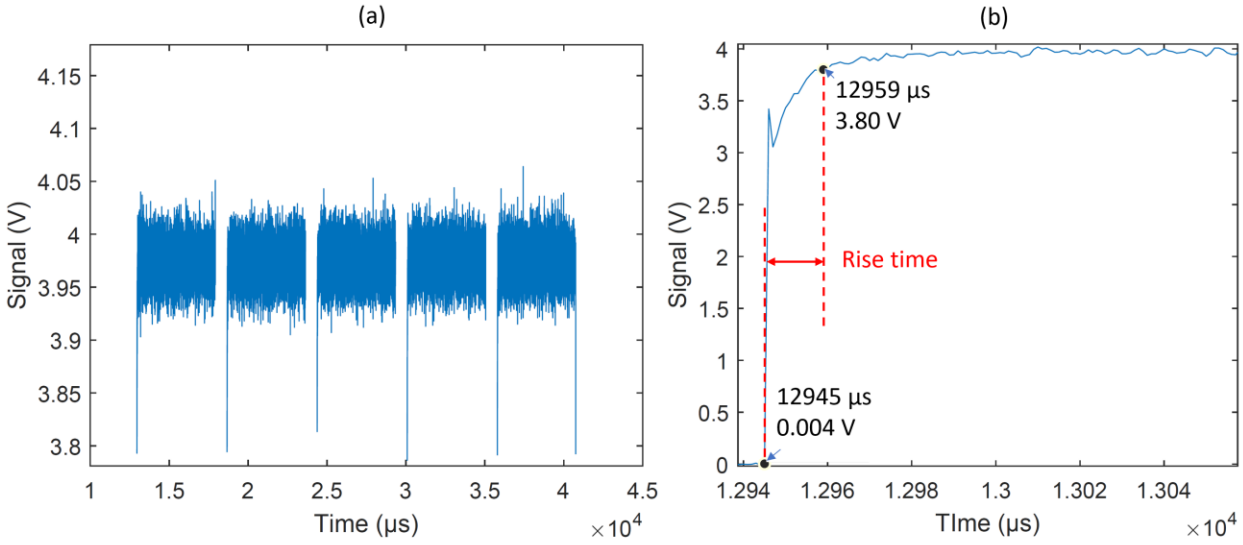

Fig. 4. PM photodiode data (taken at 1 MHz with photodiode rated for 5 MHz) from the 500 W laser operating at 285 W with (a) the signal from five tracks 5 mm long at 960 mm/s, and (b) the rise time from 0 W to 95 % of the nominal power value (271 W).

Table 1. Percent standard deviation, rise time, and fall time at four power levels of the 500 W and 1 kW lasers

	500 W			1 kW		
Power (W)	Std. dev. (%)	Rise time (μs)	Fall time (μs)	Std. dev. (%)	Rise time (μs)	Fall time (μs)
85	0.94	36	16	0.91	40	13
135	0.75	18	17	0.62	31	13
285	0.51	14	19	0.37	24	14
485	0.38	12	20	0.29	20	16

3.3. Laser beam waist position and diameter with build plane location

In order to assure that the f-theta lens properly locates the beam waist vertically relative to the fiducial plane (z-direction as illustrated in Fig. 2), the caustic must be measured in multiple locations around the build area. Measurement of the beam caustic was performed at nearly 0 W (< 1 mW) of thermal load on the optics (thermal considerations are addressed in Section 3.4), using a first-principles measurement approach of directly imaging the laser beam onto a complementary metal oxide semiconductor (CMOS) windowless focal plane array (WFPA). The requirement for a windowless FPA eliminates any assumptions about refractive index and glass thickness, which change the optical path distance to the imager. The WFPA is located relative to the fiducial plane directly using a precision laser distance finder and the Z-position is established with a stage. Then, the laser is pulsed at 100 W for very short duration (100 μs) at 5 Hz (an equivalent duty cycle of 0.05 %) while synchronously triggering the WFPA. The laser power is also attenuated a factor of more than 1×10^{10} with neutral density optical filters

directly after the beam collimator to further reduce the laser power to avoid damaging he WFPA.

The WFPA's pixel pitch was 5.5 µm per pixel and the images were fit with a 2-dimensional Gaussian curve fit to find the average beam diameter. Note that with an ideal Gaussian beam, the Gaussian diameter and the D4σ diameter are equivalent. In this study, within ± 1 mm of the beam waist, the beam is measured to have ellipticity ε > 0.97, which is well within the criteria to treat the beam as circular per ISO 11146 [12]. A forthcoming publication will extensively detail the measurement uncertainty of Gaussian beam diameters measured with a WFPA [13].

Two categories of nonidealities are in this measurement uncertainty quantification approach: beam nonidealities and measurement uncertainties [13]. The beam nonidealities include noncircular, variability around the build area, temporal variation due to heated optics, and window contamination. The measurement uncertainties include pixelation and noise, curve fit error, measurement repeatability, and Z-position accuracy. With each of these factors considered, the beam diameter standard measurement uncertainty (k = 1, Type A) is estimated to be ± 4.8 %.

In the FLaMI system, laser processing occurs at two primary locations: near normal (0 mm, 0 mm), and approximately 5° off-normal (0 mm, -55 mm). The beam caustic is shown at both of those locations in Fig. 5. Using a hyperbolic curve fit, the nominal beam waist diameter is measured to be 72 µm at 3.3 mm above the fiducial plane at the near-normal incidence location (0 mm, 0 mm) [1]. When moved to the working position at approximately 5° off-normal (0 mm, -55 mm), the beam waist shifted downward by 74 µm, which resulted in the beam diameter increasing by approximately 0.5 µm at the fiducial plane. This 0.5 µm increase in diameter is negligible in comparison to the ± 4.8 % uncertainty in beam diameter. These measurements were performed with the 500 W laser with 60 mm focal distance collimator.

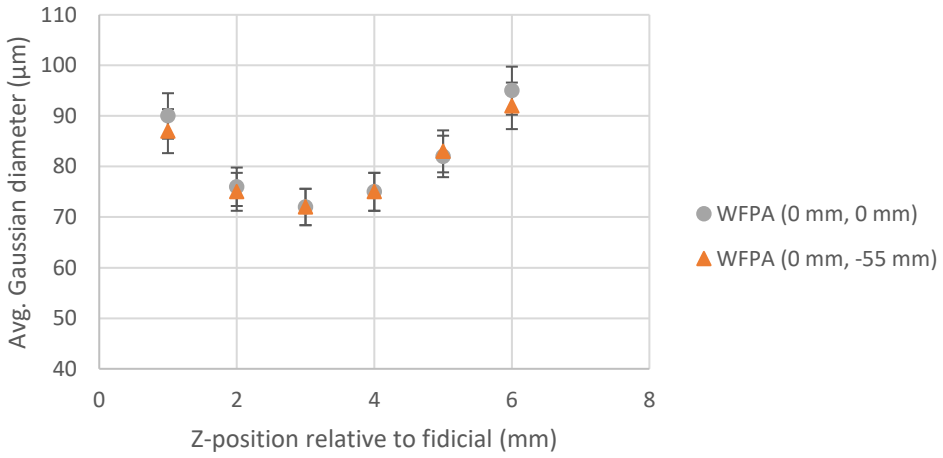

Fig. 5. Beam caustic at two working positions: near normal at (0 mm, 0 mm) and approximately 5° off-normal at (0 mm, -55 mm). The error bars are shown as standard measurement uncertainty (k = 1, Type A) of ± 4.8 %.

[1] The beam waist diameter can be adjusted from approximately 50 µm to 125 µm by swapping the laser collimator.

3.4. Thermal stability of the minimum beam waist position and diameter

The thermal stability of the beam waist position and diameter were first tested with the same configuration described in Section 3.3 with the 500 W laser and 60 mm focal distance collimator. At near-normal incidence (0 mm, 0 mm), the beam diameter and waist position were measured at two power levels with two different devices. The data in Fig. 6 from the WFPA are the same data at the near-normal position from Fig. 5, which represents negligible thermal loading of the optics (< 1 mW).

The beam caustic was additionally measured at the same location, but with 100 W applied power with x and y cross-sectional curve fits of the beam with a commercial PRIMES ScanFieldMonitor (SFM)[2] [14]. The laser exposure times were on the order of 1 ms, which is representative of typical operating conditions of the FLaMI testbed. The beam diameter standard measurement uncertainty (k = 1, Type B) of the SFM is assumed to be equivalent to the WFPA-based value of ± 4.8 %.

A hyperbolic curve fit of the data shows that from < 1 mW of applied power in pulsed mode and measured via WFPA, to 100 W of continuous applied power measured via SFM, the beam waist position shifted upward by only approximately 3 µm and a beam diameter decreased by less than 0.2 µm. This shift in diameter is negligible in comparison to the ± 4.8 % measurement uncertainty in beam diameter, and indicates the low duty cycle pulsing and neutral-density optical filters for the WFPA-based measurement have negligible spurious effects compared to the commercial SFM system.

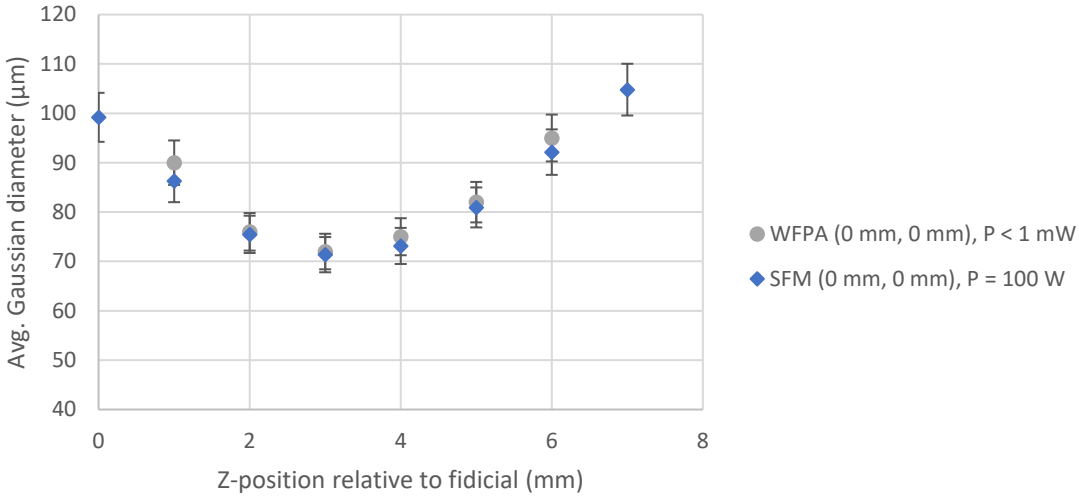

Fig. 6. Beam caustic at two applied powers: < 1 mW and 100 W. The error bars are shown as standard measurement uncertainty of ± 4.8 %.

The thermal stability of the beam waist position and diameter were further tested by outfitting the FLaMI system with a 1 kW laser with an 85 mm focal distance collimator. This combination

[2] Certain commercial equipment, instruments, or materials are identified in this paper in order to specify the experimental procedure adequately. Such identification is not intended to imply recommendation or endorsement by NIST, nor is it intended to imply that the materials or equipment identified are necessarily the best available for the purpose.

changes nominal location of beam waist relative to fiducial plane to -0.5 mm but maintains the nominal beam diameter of 72 µm. In this configuration, the beam caustic was measured with the SFM at 100 W and 1 kW at near-normal, as well as at approximately 6° off-normal (0 mm, -65 mm) at 100 W, as shown in Fig. 7. Hyperbolic curve fitting of the 100 W and 1 kW tests indicated a downward beam waist shift of 105 µm, increasing the beam diameter at the fiducial plane by 0.8 µm. Furthermore, when measured at the approximately 6° off-normal position at 100 W, the beam diameter shifted by less than 0.2 µm, further confirming that the f-theta lens adequately compensates the beam waist position at off-normal working positions. Similarly with the previous sections, these shifts in position and diameter are negligible in comparison to the ± 4.8 % measurement uncertainty in beam diameter.

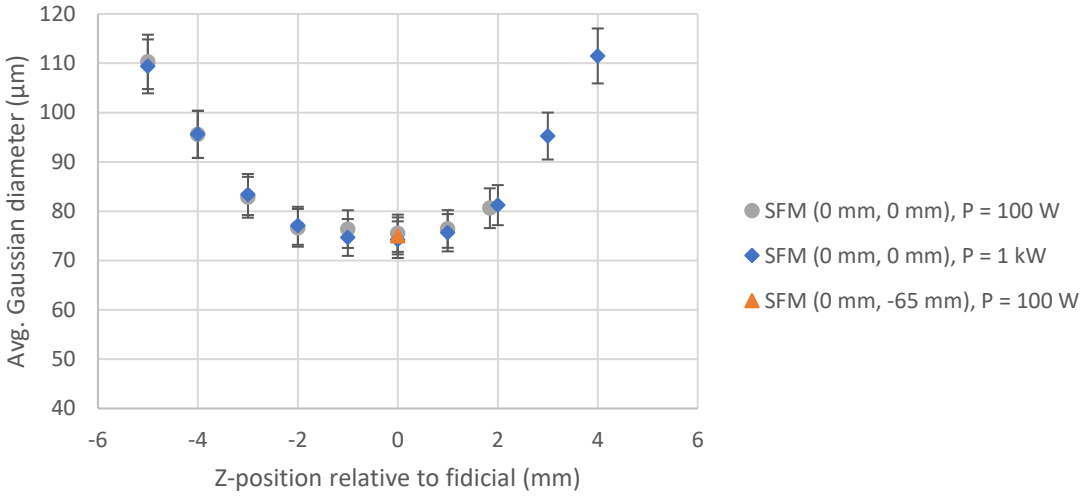

Fig. 7. Beam caustic at two applied powers and two positions: 100 W and 1 kW near normal, and 100 W at approximately 6° off-normal (0 mm, -65 mm). The error bars are shown as standard measurement uncertainty (k = 1, Type B) of ± 4.8 %.

3.5. Positioning and trajectory accuracy

The positioning and trajectory accuracy were tested by directly imaging the laser beam location with a high-speed camera at the laser wavelength. A custom target was developed for this application, which consisted of a polytetrafluoroethylene film on top of a black anodized aluminum base. The film produced a diffuse reflection of the beam that could be imaged, while the aluminum base diffused the laser heating. The beam, with applied power of 100 W and scan speed of 960 mm/s, was imaged at 48 kHz. The imaging configuration is illustrated in Fig. 2. The resulting images were thresholded at 95% of the peak signal value and the centroid of the binary image sequence was tracked from frame to frame to locate the laser beam, with results illustrated in Fig. 8.

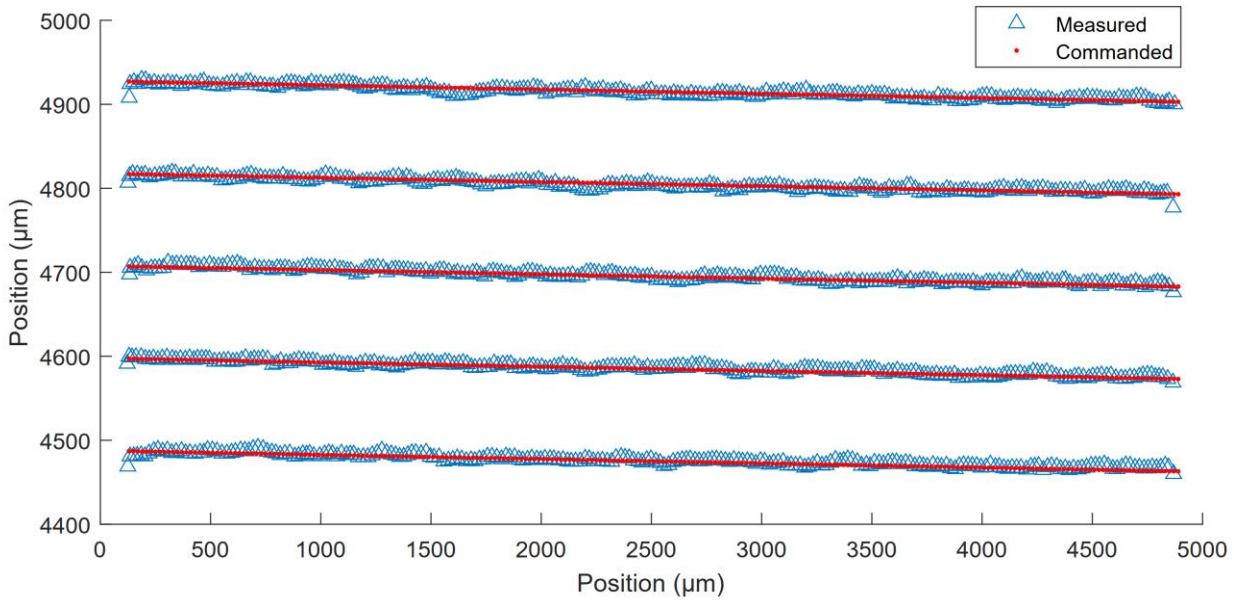

Fig. 8. Measured beam location compared with the commanded position.

As shown, the maximum linear distance deviation of the measured position from the commanded position in a five-track, raster-scanned pad (the first track scans left to right and each subsequent track alternates) is approximately 41 µm. The maximum deviations occur at the initiation and termination of the tracks due to imperfect synchronization of the laser with the galvo. Note that at higher laser powers, the rise time reduces and will result in reduced initial position deviation. In any case, the maximum deviation is approximately half the acceptable value indicated in ISO/ASTM 52941:2020(E) [10]. The root-mean squared position deviation was 21 µm and the jump speed from termination of one track to the initiation of the next with 110 µm hatch spacing at 960 mm/s is 0.75 ms.

3.6. Scanning speed accuracy

The data from Section 3.5 were also used to calculate the scan speed accuracy by calculating cumulative distance with time and then taking the speed as the slope of the linear regression between cumulative distance and time. The resulting calculated speed was 950.5 mm/s, or approximately 1 % less the commanded value. In comparable tests at a later date, the ScanFieldMonitor consistently calculated a speed to be 1 % greater than the commanded value. On a third date, the scan speed was measured by imaging the guide beam with the processing laser off. Using the same image processing approach described previously, the measured velocity was repeatably 961 mm/s. And so, it is assumed that the typical scanning speed lies in between these two most extreme measured values in a rectangular probability, which results in a standard measurement uncertainty (k = 1, Type B) of ±0.6 % [15].

4. Mechanical positioning

The majority of mechanical function tests outlined in ISO/ASTM 52941:2020(E) [10] do not apply to the FLaMI system because the experimental testbed is designed for laser melting on bare plates or with a single layer of powder at a time. Nevertheless, a few items should be noted in comparison to an industrial build machine:

- The build plane is defined by the beam waist position, which is referenced relative to the fiducial plane described in Section 5, Section 3.3, and Section 3.4.
- Precision thickness shims are used to guide a hand-held spreading blade for application of a single layer of powder. The shim thickness locates the maximum powder particle height relative to the sample with an estimated standard uncertainty (k = 1, Type B) of ± 10 µm.
- The build platform is not heated due to potential detriments to sensitive metrology.

5. Gas flow and oxygen content

The FLaMI inert gas flow system relies on a purge configuration with a small enclosure (< 18 L), in which more inert gas (argon or nitrogen) is fed into the inlet than is extracted from the outlet (through a high-efficiency particulate air filter), with both the inlet and outlet having mass flow meters. The enclosure is not a tightly sealed pressure vessel. And so, in this way, a vacuum chamber is not needed, which allows for significant metrological flexibility in the large space around the laser-matter interaction volume. The outlet gas is sampled with a commercial oxygen sensor that is periodically compared against other oxygen sensors. Typical oxygen levels in the FLaMI system are less than 500 ppm when properly purged.

The gas flow speed profiles and their associated measurement uncertainties were measured at four volumetric flow rates with the same method described in Weaver et al. [16], as shown in Fig. 9. The gas flow plenums were designed such that at 60 LPM, the gas flow profile approximates that of the Additive Manufacturing Metrology Testbed (AMMT) from AM-Bench 2022. In the FLaMI system, the gas flow is generally in the positive-Y direction (coordinates shown in Fig. 2). The hot wire anemometer was positioned at +10 mm and -10 mm in the x-direction (covering a typical 25 mm × 25 mm sample centered on 0 mm, 0 mm), and measured flow speed variance under nominally steady-state conditions was found to be less than ± 5 %, which is significantly less than the gas flow speed measurement uncertainty of ±10 % (k = 1, Type B) with argon as the inert gas. As described in Weaver et al. [16], the largest component of gas speed measurement uncertainty is the derivation of a correction factor from the anemometer's air speed measurement calibration to the speed of argon. It should be noted that the sample is always centered within the enclosure, even at off-normal working positions, which means that the gas flow speed profiles remain constant at the test sample.

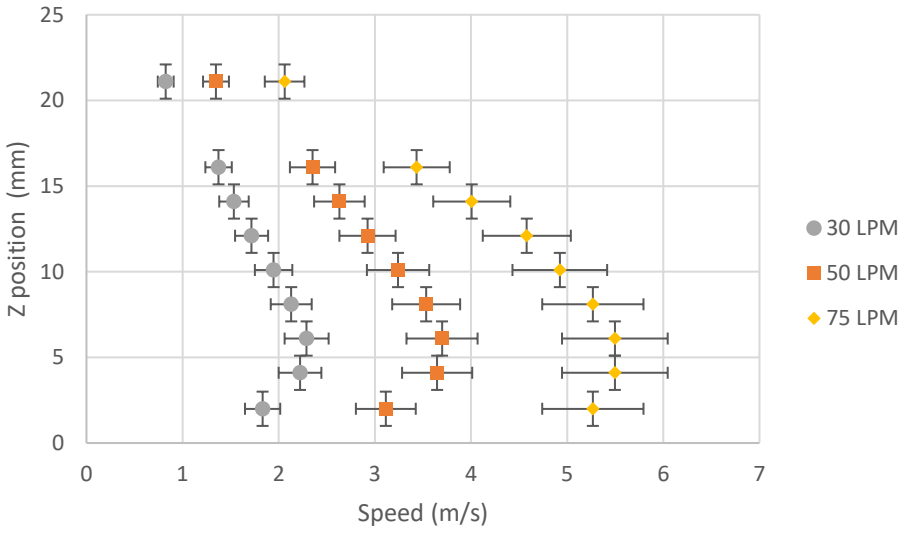

Fig. 9. Gas flow speed profiles with argon at four volumetric flow rates. Horizontal error bars represent the standard uncertainty of the measured flow speed, and vertical bars are the positioning uncertainty of the anemometer positioning stage.

6. Summary

A novel laser processing testbed has been developed to study fundamental aspects of laser-matter interaction in support of machine qualification, model validation, and process monitoring research. A primary objective of development of this testbed was to assure highly accurate and well-characterized laser melting conditions. Design considerations for the system are first summarized. Next, the document loosely follows the structure and recommended "acceptance tests" per ISO/ASTM 52941:2020(E) [10].

In the laser power calibration, two types of power metrology (thermal PM and PM photodiode) are described and used to span the power range from 70 W to 1 kW. The PM photodiode was used to assess power stability and rise/fall time. Two measurement methods (low-duty cycle direct imaging and a commercial patterned glass device) are then used to assess laser beam waist position and diameter with varying position around the build area. The thermal stability of the minimum beam waist position and its diameter are similarly assessed. The laser positioning, trajectory accuracy, and scanning speed are directly measured using a high-speed camera to directly locate the laser on a custom target. Finally, the mechanical positioning, gas flow, and oxygen content measurements are described. Overall, the FLaMI testbed has shown excellent performance in terms of accuracy and repeatability, as summarized in Table 2.

Table 2. Summary of the FLaMI testbed performance.

	Measurement results	**Description**	**Operation range**
Laser power	±2.5 %	Meas. Unc., Type B, k = 1	70 W to 1000 W
Laser power stability	±1 %	Standard deviation	-
Laser power rise/fall time	< 40 µs	-	-
Gaussian beam diameter	±4.8 %	Meas. Unc. at beam waist, Type A, k = 1	72 µm in this study, approx. 50 µm to ≥125 µm with different collimators
Beam waist position	105 µm	Max. dev.	-
Positioning and trajectory accuracy	41 µm	Max. dev.	-
	±21 µm	RMSE	-
Jump speed	≥ 0.75 ms	With 110 µm hatch spacing scanned at 960 mm/s	-
Scanning speed accuracy	± 0.6 %	Meas. Unc., Type B, k = 1	< 14 m/s with a single track* < 2 m/s with a pad**
Oxygen content	< 500 ppm	-	-
Gas flow speed	±10 %	Meas. Unc., Type B, k = 1, with argon	< 5.5 m/s at 5 mm above the build plane

*Tested for single tracks only

**Maximum speed tested for raster-scanned pads with 110 µm hatch spacing

7. Acknowledgements

The authors thank Shawn Moylan, Brandon Lane, and Jordan Weaver for their support in development of the FLaMI testbed.

References

[1] Yadroitsev I, Yadroitsava I, Du Plessis A, MacDonald E (2021) *Fundamentals of laser powder bed fusion of metals* (Elsevier).

[2] Levine L, Lane B, Glaessgen E, Gorelik M (2024) Providing a Rigorous Benchmark Measurement Foundation for Modeling-Informed Qualification and Certification of Metal Additive Manufactured Components. *JOM* 76(4):1897–1904. https://doi.org/10.1007/s11837-024-06388-7

[3] McCann R, Obeidi MA, Hughes C, McCarthy É, Egan DS, Vijayaraghavan RK, Joshi AM, Acinas Garzon V, Dowling DP, McNally PJ, Brabazon D (2021) In-situ sensing, process monitoring and machine control in Laser Powder Bed Fusion: A review. *Additive Manufacturing* 45:102058. https://doi.org/10.1016/j.addma.2021.102058

[4] Deisenroth D, Mekhontsev S, Lane B, Hanssen L, Zhirnov I, Khromchenko V, Grantham S, Cardenas-Garcia D, Donmez A (2021) Measurement Uncertainty of Surface Temperature Distributions for Laser Powder Bed Fusion Processes. *Journal of Research of NIST* 126. https://doi.org/10.6028/jres.126.013

[5] Deisenroth DC, Mekhontsev S, Lane S (2020) Measurement of mass loss, absorbed energy, and time-resolved reflected power for laser powder bed fusion., Proc. SPIE 11271, Laser 3D Manufacturing VII, p 112710L. https://doi.org/10.1117/12.2547491

[6] Wittemer M, Ferle F, Wudy K (2024) In-line process monitoring in laser welding and powder bed fusion of metals using directional reflection measurements. *Journal of Laser Applications* 36(4):042025. https://doi.org/10.2351/7.0001559

[7] Huang W, Deisenroth D, Mekhontsev S, Tan W (2023) Correlation between keyhole geometry and reflected laser light distribution in laser-based manufacturing. *Manufacturing Letters* 38:56–59. https://doi.org/10.1016/j.mfglet.2023.09.002

[8] Bidare P, Bitharas I, Ward RM, Attallah MM, Moore AJ (2018) Fluid and particle dynamics in laser powder bed fusion. *Acta Materialia* 142:107–120. https://doi.org/10.1016/j.actamat.2017.09.051

[9] Deisenroth DC, Neira J, Weaver J, Yeung H (2020) Effects of Shield Gas Flow on Meltpool Variability and Signature in Scanned Laser Melting. *MSEC2020* (Volume 1: Additive Manufacturing; Advanced Materials Manufacturing; Biomanufacturing; Life Cycle Engineering; Manufacturing Equipment and Automation). https://doi.org/10.1115/MSEC2020-8410

[10] ISO/ASTM (2020) *52941 – Additive manufacturing — System performance and reliability — Acceptance tests for laser metal powder-bed fusion machines for metallic materials for aerospace application* (ISO/ASTM).

[11] ISO (2017) *11554 – Optics and photonics — Lasers and laser-related equipment — Test methods for laser beam power, energy and temporal characteristics* (ISO).

[12] ISO (2021) *11146-1 – Lasers and laser-related equipment — Test methods for laser beam widths, divergence angles and beam propagation ratios* (ISO).

[13] Deisenroth D, Weaver J, Mekhontsev S, Grantham S, Moylan S (2025) Laser Beam Metrology for AM-Bench 2022: Approaches, Results, and Lessons Learned. *In review to NIST Advanced Manufacturing Series*.

[14] Koglbauer A (2018) More Than Beam Profiling: A new approach for beam diagnostics in 3D additive manufacturing systems. *Laser Technik Journal* 15(3):40–44.

[15] Taylor BN, Kuyatt CE (1994) Guidelines for evaluating and expressing the uncertainty of NIST measurement results. *National Institute of Standards and Technology*, NIST Technical Note 1297.

[16] Weaver J, Schlenoff A, Deisenroth D, Moylan S (2021) Inert Gas Flow Speed Measurements in Laser Powder Bed Fusion Additive Manufacturing. *NIST Advanced Manufacturing Series.* https://doi.org/10.6028/NIST.AMS.100-43

[17] Zhirnov I, Mekhontsev S, Lane B, Grantham S, Bura N (2020) Accurate determination of laser spot position during laser powder bed fusion process thermography. *Manufacturing Letters* 23:49–52. https://doi.org/10.1016/j.mfglet.2019.12.002

Appendix A Exemplary In-Situ Metrology

This appendix provides examples of some of the in-situ metrology configurations that can be utilized in the FlaMI system. Section A. 1. shows the metrologies that are used to quantify laser beam power density distribution and scanning speed. Section 0. through Section A. 4. provide examples of the in-situ metrology used to measure physical characteristics of the laser-matter interaction.

A. 1. Laser beam metrology

As discussed in this document, one of the major focuses of the FLaMI system is accurate characterization of the laser beam. As shown in Fig. 10, the FLaMI system has provisions for three beam profiling instruments, including the PRIMES ScanFieldMonitor, a calibrated beam sampler, and a WFPA (operated with low beam power).

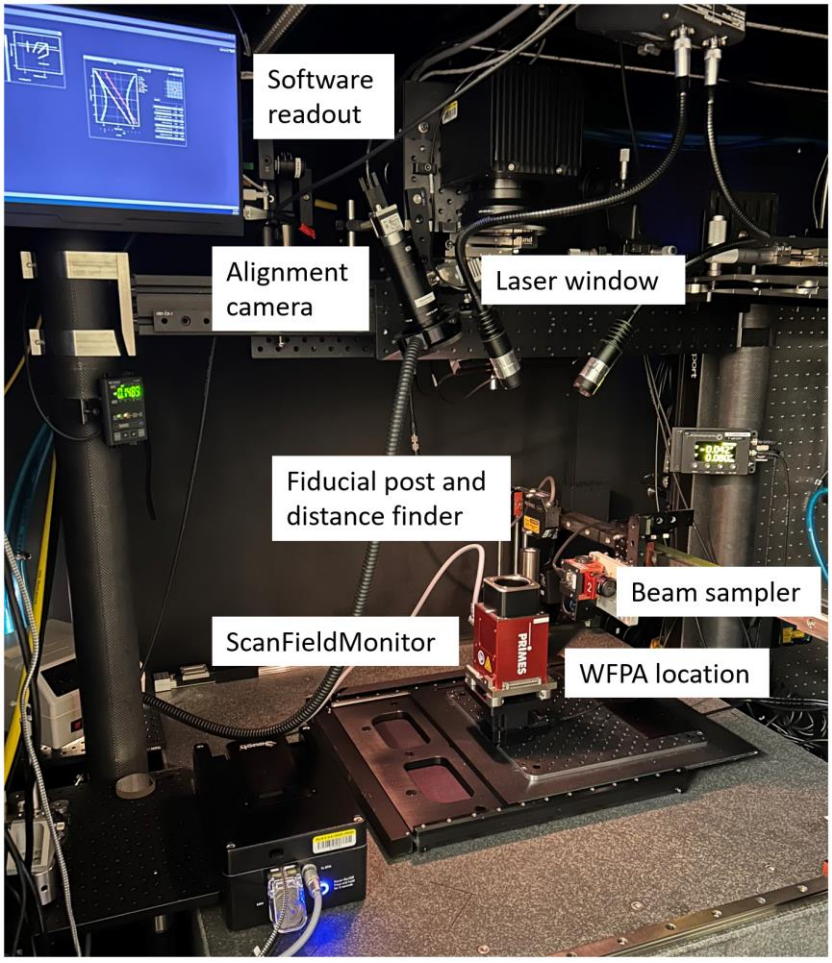

Fig. 10. Laser beam metrology within the FLaMI system.

The beam profiling devices are positioned relative to the build plane using the fiducial post and the laser distance finder mounted on an X-Y gantry. A laser window is placed in the beam path as would be in place with a gas flow enclosure under normal laser processing conditions. An

alignment camera and software readout screen aid with device positioning and data acquisition.

A. 2. Laser coupling and directionally resolved reflected laser distributions

Two types of reflected laser metrology can be implemented using a “registration dome.” The first setup uses a dome that is internally coated diffuse white so that the total reflected laser power is integrated and can be measured with a photodetector temporally at ≥ 1 MHz. The fraction of the applied power that is reflected can then be used to calculate the dynamic laser coupling, which is a useful input or validation metric for multiphysics models of the laser-matter interaction [5].

The second setup uses a dome that is internally coated diffuse grey (reflectance of approximately 13 %) so that the total reflected laser power minimally integrated within the dome. This allows for the reflected power distributions to be imaged with a 180° fisheye lens, and thus, directionally resolved. The fisheye imager has demonstrated temporal resolution of up to 60 kHz. These high-speed directionally resolved laser power distributions provide a new high-fidelity model validation approach [6], as well as support of a novel and highly-promising process monitoring approach [7].

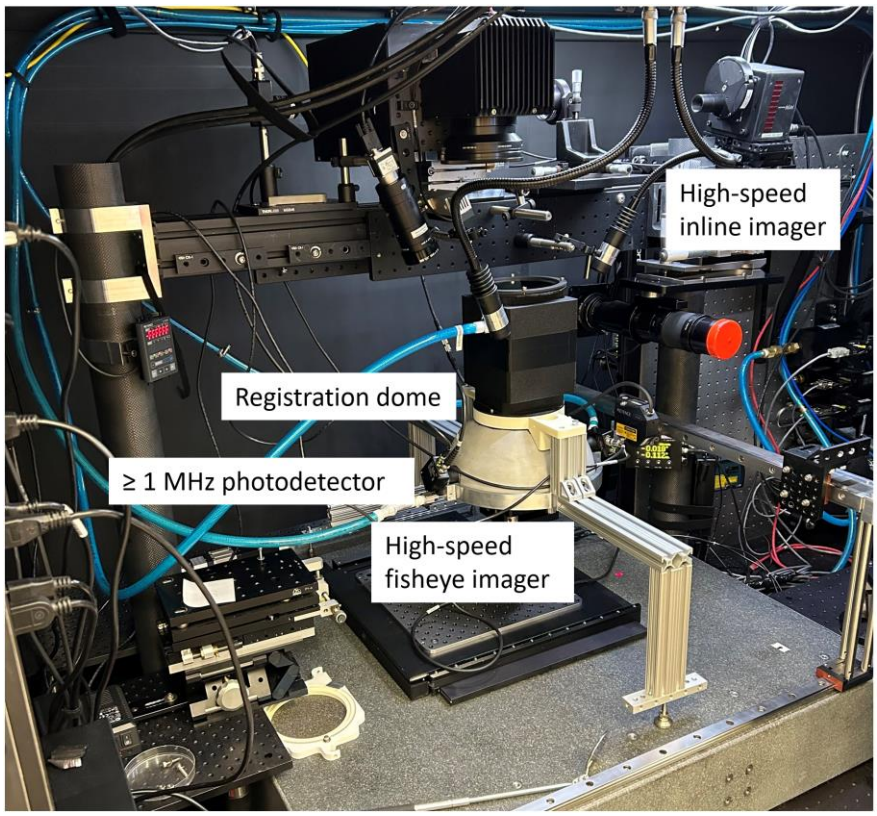

Fig. 11. Experimental setup for laser coupling and directionally resolved reflected laser distributions metrology.

A. 3. High-speed and high magnification thermography and backlit plume/ejecta imaging

The FLaMI system can be outfitted with a high-speed and high magnification thermographic camera, as shown in Fig. 12. The imager is capable of measuring (radiance) temperatures ranging from 850 °C to more than 1200 °C at 48 kHz with pixel resolution of 14.3 µm/pixel. This allows for measurement of material cooling rates (which drive microstructure and mechanical properties), as well as the dynamics of hot ejecta.

Simultaneously, the FLaMI system can be outfitted with a high-speed and high magnification backlit (or non-backlit) plume/ejecta imagers. The horizontal viewing angle and orthogonal perspectives of two additional high-speed imagers allow for 3-dimensional measurements of the plume structure, as well as measurement of ejecta sizes, quantities, and velocities. The horizontal view cameras have demonstrated imaging speeds of 67.5 kHz with resolution of 14.5 µm/pixel. By implementing varying bandpass filters in the imagers, this configuration can also be used to measure spectral properties of the process plume. The properties of the plume and ejecta have important ramifications for in-process monitoring, in addition to the quality/porosity of built parts.

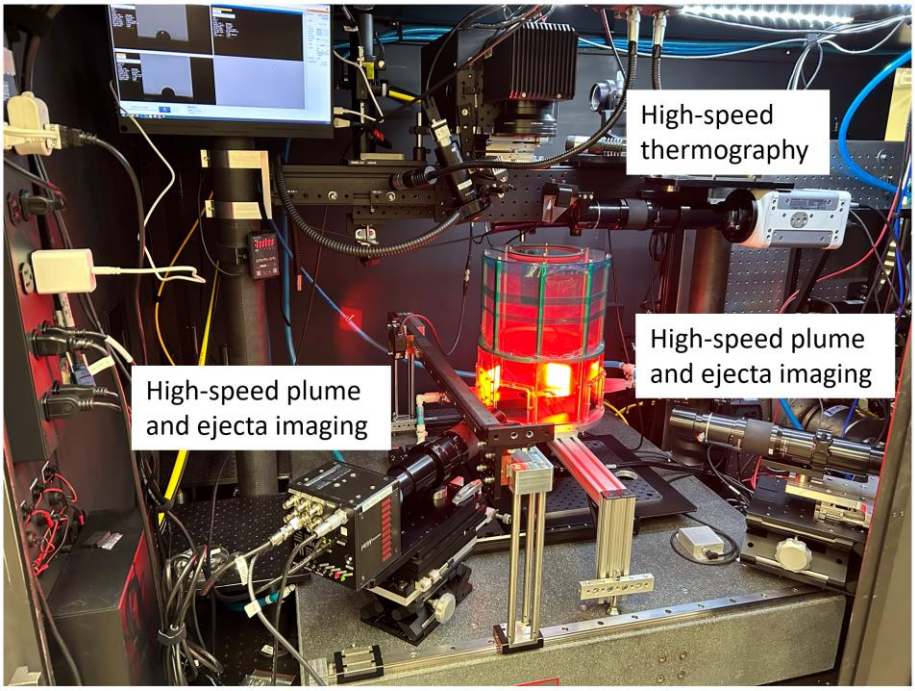

Fig. 12. Experimental setup high-speed and high magnification backlit plume and ejecta imaging.

A. 4. High-speed and very-high magnification melt pool imaging with process laser tracking

High-speed and high magnification melt pool imaging provides important insights into the dynamics of laser-matter interaction, particularly the melting dynamics of powder and the associated process ejecta. As shown in Fig. 13 the FLaMI system can be equipped with a high-speed imager with sampling frequency demonstrated up to 150 kHz with magnification of 1.8 µm/pixel, allowing for outstanding visualization of the melt pool and powder dynamics. Such

high-speed and high magnification requires intense illumination of the scene, which is achieved by a 1 W local illumination laser. Furthermore, the location of the processing laser can be tracked with inline laser illumination, allowing for measurement of powder and melt pool dynamics relative to the position of heat input [17]. Finally, high-resolution macroscale images of the powder bed before and after melting can be produced with 2.0 µm/pixel resolution over an 8.5 mm × 8.5 mm field of view (20 megapixel (MP) macro-view).

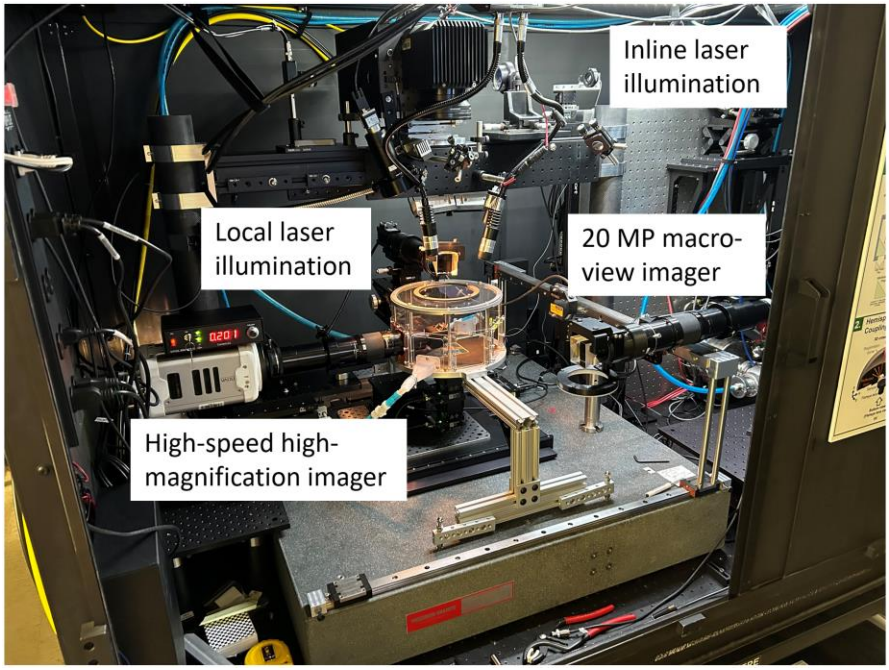

Fig. 13. Experimental setup high-speed and very-high magnification melt pool imaging with process laser tracking.